



Angular dependence of aerosol information content in CAPI/TanSat observation over land: Effect of polarization and synergy with A-train satellites

Xi Chen^{a,b,c,*}, Jun Wang^{c,d,**}, Yi Liu^a, Xiaoguang Xu^{c,d}, Zhaonan Cai^a, Dongxu Yang^a, Chang-Xiang Yan^e, Liang Feng^f

^a Key Laboratory of Middle Atmosphere and Global Environment Observation, Institute of Atmospheric Physics, Chinese Academy of Sciences, Beijing 100029, China

^b University of Chinese Academy of Sciences, Beijing 100049, China

^c Earth and Atmospheric Sciences, University of Nebraska-Lincoln, 303 Bessey Hall, Lincoln, NE 68588, USA

^d Center for Global and Regional Environmental Research, Department of Chemical and Biochemical Engineering, The University of Iowa, 4133 Seamans Center, Iowa City, IA 52242, USA

^e Changchun Institute of Optics, Fine Mechanics and Physics, Chinese Academy of Sciences, Changchun 130033, China

^f National Centre for Earth Observation, School of GeoSciences, University of Edinburgh, UK

ARTICLE INFO

Article history:

Received 7 October 2016

Received in revised form 14 April 2017

Accepted 8 May 2017

Available online 12 May 2017

Keywords:

CAPI

Aerosol

Information content

Retrieval error

DFS

ABSTRACT

Aerosols affect the radiative transfer in the absorption bands of carbon dioxide (CO₂), thereby contributing to the uncertainties in the retrieval of CO₂ from space. A Cloud and Aerosol Polarimetric Imager (CAPI) has been designed to fly on the Chinese Carbon Dioxide Observation Satellite (TanSat) and provide aerosol and cloud information to facilitate the measurements of CO₂. This study aims to assess the information content about aerosol properties that can be obtained from CAPI's observations of radiance and polarization. We simulate synthetic CAPI observations using the UNified Linearized Vector Radiative Transfer Model (UNL-VRM), from which the degree of freedom for signal (DFS) and *a posteriori* error for various aerosol parameters are calculated using optimal estimation theory. The simulation considers different combinations of fine and coarse aerosols and includes detailed treatment for both soil and vegetation surfaces. It is found that CAPI can provide 3 to 4.5 independent pieces of information about aerosol parameters, mainly related to aerosol total volume (or aerosol optical depth), fine mode fraction (fmf_v) of aerosol volume, and imaginary part of refractive index for coarse mode aerosols. At directions around back-scattering, aerosol information content is smaller due in part to the large directional surface reflectance. In addition, aerosol DFS also depends on fmf_v, aerosol optical depth and solar zenith angle, and such dependence is analyzed for various viewing and azimuth angles. Due to weaker scattering of coarse aerosol, the information content of large particle is relatively less. Therefore, as fmf_v decreases, DFS remains large for fine aerosol and increases for coarse aerosol. With larger aerosol optical depth (AOD), more aerosol information content can be obtained, but when AOD increases to a threshold ranging from 0.5 to 1.2, aerosol DFS doesn't increase any more. At larger solar zenith angles (SZA), a longer light path affected by aerosol can slightly increase aerosol information content. Furthermore, the degree of linear polarization (DOLP) is shown to be more sensitive to aerosol properties than reflectance, hence improves CAPI's aerosol retrieval accuracy. The additional information content raised from DOLP measurements ranges from 1 to 1.8 in terms of DFS and reaches the largest in conditions of 0.2 < fmf_v < 0.4 at SZA < 60°. The larger AOD and fmf_v, the more improvement for characterizing fine aerosol is obtained from polarization due to larger DOLP of fine aerosol scattering (or less for coarse aerosol). If AOD is known *a priori* (for example, from other A-Train satellites), total DFS for aerosol information content can be improved by 0.8 to 1.6 in most cases, and could exceed 2.0 for conditions of small AOD (<0.2). However, the improvement has little dependence on AOD if AOD is larger than 0.2.

© 2017 Elsevier Inc. All rights reserved.

* Correspondence to: X. Chen, Key Laboratory of Middle Atmosphere and Global Environment Observation, Institute of Atmospheric Physics, Chinese Academy of Sciences, Beijing 100029, China.

** Correspondence to: J. Wang, Earth and Atmospheric Sciences, University of Nebraska-Lincoln, 303 Bessey Hall, Lincoln, NE 68588, USA.

E-mail addresses: chenxiliao@mail.iap.ac.cn (X. Chen), jun-wang-1@uiowa.edu (J. Wang).

1. Introduction

Carbon dioxide (CO₂) is one of the most important greenhouse gases and its concentration has increased from 279 ppm in 1750 to 391 ppm in 2011, with the accelerated increase rate since the beginning of 21 century (Pachauri et al., 2014). To monitor the global CO₂ and

understand its sources and sinks at a global scale, a few satellite missions have been deployed or planned, such as the Greenhouse gases Observing SATellite (GOSAT) launched on January 2009 (Kuze et al., 2009; Yokota et al., 2009), the Orbiting Carbon Observatory-2 (OCO-2) launched on 2 July 2014 (Boesch et al., 2011), and the Chinese Carbon Dioxide Observation Satellite (TanSat) just launched on UTC 19:22, 21 December 2016 (Liu et al., 2013). The main objective of the TanSat mission is to retrieve the atmosphere column-averaged CO₂ dry air mole fraction (X_{CO_2}) with the precision of better than 1% (4 ppm) in order to meet the requirement of characterizing CO₂ sources and sinks on national and regional scales. TanSat flies in a sun-synchronous orbit at 13:30 h, with a shorter than 16-day ground-track repeat time. This satellite is able to carry out nadir and target observations over land and sun-glint observations over ocean. A high-resolution Carbon Dioxide Spectrometer (CDS) on TanSat is designed to measure reflected sunlight in the 0.76- μ m O₂ A-band and in the CO₂ bands at 1.61 μ m and 2.06 μ m. However, aerosols scattering and absorption could induce non-ignorable interference in the radiative transfer of CO₂ absorption band, thereby increasing errors in the retrieval of columnar CO₂ amount from satellite measurements (Aben et al., 2007; Butz et al., 2009; Houweling et al., 2005). Hence, these CO₂-focused satellites also carry instruments to measure aerosol and cloud properties to compensate errors for operational CO₂ retrieval algorithms. For example, the Cloud and Aerosol Imager (CAI) on GOSAT measures radiance at 380, 678, 870, 1640 and 1620 nm. Comparing to the CAI that only measures radiances, the Cloud and Aerosol Polarimetric Imager (CAPI) on TanSat is a wide field of view (FOV) moderate resolution imaging spectrometer that can simultaneously measure radiances in five atmospheric window bands (380, 670, 870, 1375, and 1640 nm) as well as polarization in a visible band (670 nm) and a NIR band (1640 nm). As the first part of a series of studies that aim to develop an aerosol retrieval algorithm for CAPI, this paper is to assess the retrieval capability of CAPI observations for various aerosol parameters.

Past remote sensing of aerosols has used radiances at atmospheric window channels to retrieve aerosol optical depth (AOD), including the Moderate Resolution Imaging Spectroradiometer (MODIS) Dark Target algorithm that uses 670 and 2100 nm (Kaufman et al., 1997; Levy et al., 2007), the MODIS and Sea-viewing Wide Field of view Sensor (SeaWiFS) Deep-Blue algorithm based on 412 nm, 470 nm and 650 nm (or 412 nm, 490 nm and 670 nm for SeaWiFS) (Hsu et al., 2004, 2006; Hsu et al., 2013), the Ozone Monitoring Instrument (OMI) aerosol algorithm that utilizes 354 nm and 388 nm (Torres, 2005; Torres et al., 1998; Torres et al., 2007), and the Medium Resolution Imaging Sensor (MERIS) aerosol algorithm focusing on blue wavelengths (von Hoyningen-Huene et al., 2003). Either the lower surface reflectance at shorter wavelength such as UV or blue band, or relationship of surface reflectance between visible and NIR is utilized by these algorithms to separate aerosol information from surface reflection. The use of multi-spectral radiance measurements in these algorithms allows a characterization of aerosol loading with not only AOD but also other properties such as Angstrom Exponent (AE), aerosol index (AI), and fine mode aerosol fraction (fmf).

One of unique features of CAPI is that it measures reflectance from UV to NIR as well as DOLP, which are expected to have potential for the retrievals of multiple pieces of aerosol information (in addition to AOD). The DOLP of backscattered solar radiation is sensitive to the change of aerosol properties (Herman et al., 1997) as the polarized reflectance by surface is often small (Maignan et al., 2009; Nadal and Breon, 1999). Thus, the relative contribution of aerosols to polarized component of the top-of-the-atmosphere (TOA) reflectance is much higher than that for the total reflectance, which makes it easier to derive aerosol properties from polarized sensors like the Polarization and Directionality of Earth Reflectance (POLDER) (Deuzé et al., 2001; Herman et al., 1997). From the multi-spectral, multi-angle polarimetric measurements, some studies have demonstrated the possibility to derive more detailed information about aerosol properties including the

particle size distribution, complex refractive index, and parameters characterizing aerosol particle shape and vertical distribution (Dubovik et al., 2011; Kokhanovsky et al., 2007; Kokhanovsky et al., 2010; Xu et al., 2015). Based on these studies, it is expected that CAPI measurements have the potential for retrieval of aerosol properties in addition to AOD.

However, to our knowledge there has been no algorithm combining UV, visible, and NIR reflectance together with polarization to retrieve aerosol properties. The most similar algorithm is the one for POLDER on PARASOL with the spectral ranges from blue bands to NIR (Deuzé et al., 2001). Hence, it is necessary to assess the aerosol information content of CAPI measurement and thereby provide guidance for designing and implementing a practical retrieval algorithm. To this end, we conduct a theoretical information content analysis using synthetic data for CAPI. Based on optimal estimation theory, our analysis provides how much information content for each aerosol parameter is possibly available in the CAPI measurements. Previous studies have shown that aerosol information content in the satellite measurement depends on aerosol and surface type and observation geometry (Holzer-Popp et al., 2008; Martynenko et al., 2010; Wang et al., 2014). But these studies focused on the radiance-measurements only, and this study differs from these past studies in the following aspects. First, this study extends the framework of our past study on information content analysis for the ground-based measurements (e.g., Aerosol Robotic Network, Xu and Wang, 2015) to the satellite observation, and therefore, the angular effect from surface bi-direction reflectance function becomes important and is specifically analyzed in this study. Second, this study uses the formal optimization theory (Rodgers, 2000) to not only quantify the information content of aerosols in terms of degree of freedom for signals (DFS) but also estimate posterior error for each retrieved parameter, not only for fine-mode but also for coarse-mode aerosols at all possible Sun-Earth-Satellite viewing geometries; such analysis has not been done before, especially for CAPI-type of instruments that combine UV, visible, and NIR reflectance together with polarization. Finally, this study also analyzes the synergy between CAPI with other A-train satellites. Therefore, the new development of our method and the comprehensive analysis of aerosol information content for CAPI enable us to reveal, for the first time, how a combination of reflectance and polarization in UV, VIS, and NIR channels can improve the characterization of aerosols beyond AOD.

Quantitatively, the purpose in this paper is to investigate what aerosol parameters can be possibly retrieved from CAPI observations and how accurate the retrievals are. The multispectral reflectance and DOLP to be measured by CAPI are simulated by the Unified Linearized Vector Radiative Transfer Model (UNL-VRM) developed by (Wang et al., 2014). The outputs of this forward model, including not only Stokes vector but also the Jacobians of the Stokes vector with respect to aerosol scattering and microphysical parameters, are used to quantify the information content in terms of both degree of freedom for signal (DFS) and retrieval uncertainty for each parameter. In addition to evaluate which aerosol parameters can be retrieved, we also quantify the amount of aerosol information content that is enhanced with the addition of CAPI's DOLP measurements. Furthermore, the angular dependence of aerosol information content is analyzed to estimate the impact of observation geometry on the retrieval accuracy. Finally, we assess how the AOD from A-train satellite could help to augment CAPI's aerosol retrievals. Although similar analysis about polarization and angular dependence has been explored in other sensors, such as POLDER or MISR, the focus in this study is to conduct quantitative analysis for CAPI, especially its information content for aerosol parameters (such as size and refractive index). The information content analysis in this study will provide a theoretical foundation for developing a CAPI operational algorithm for the aerosol retrievals.

Section 2 describes the theory of information content analysis. The numerical simulation of CAPI reflectance and DOLP as well as key assumptions made in our analysis are introduced in Section 3. The results

from aerosol information content analysis, especially the impact of DOLP for aerosol characterization, are presented in Section 4. In Section 5, we focus on analysis of aerosol information content of CAPI's nadir observations (e.g., CAPI's normal observation mode) and the variation of the aerosol information content with the solar zenith angle. In Section 6, we discuss the improvement of aerosol information content and retrieval accuracy through synergetic use of AOD (from A-train satellite) and CAPI measurements. Finally, we summarize this paper and discuss the future plan in Section 7.

2. Information content analysis theory

Let \mathbf{x} a state vector consisting of n parameters (such as AOD) to be retrieved from an observation vector \mathbf{y} containing m elements of measurements (such as spectral reflectance and polarization). The relationship between \mathbf{y} and \mathbf{x} can be expressed by

$$\mathbf{y} = \mathbf{F}(\mathbf{x}) + \epsilon, \quad (1)$$

where the forward model \mathbf{F} describes the physical processes that link the measurements to the state vector. ϵ represents the combined errors from both the observation process and forward modeling, and hereafter, is called measurement error for simplicity.

The inversion problem is to infer the state vector from the measurements. Assuming that errors follow a Gaussian probability density function and observation vector is linearly related to the state vector at the vicinity of the true state, we can get the optimal estimation of the state vector:

$$\hat{\mathbf{x}} = \mathbf{x}_a + \left(\mathbf{K}^T \mathbf{S}_\epsilon^{-1} \mathbf{K} + \mathbf{S}_a^{-1} \right)^{-1} \mathbf{K}^T \mathbf{S}_\epsilon^{-1} (\mathbf{y} - \mathbf{K} \mathbf{x}_a), \quad (2)$$

where \mathbf{S}_a represents the error covariance matrix for the prior state vector, \mathbf{x}_a , and \mathbf{S}_ϵ is the measurement error covariance matrix. \mathbf{K} is called weighting function matrix or Jacobian matrix, and comprised of the partial derivative of each forward model element with respect to every state vector element, i.e. $K_{i,j} = \partial F_i / \partial x_j$ ($K_{i,j}$ represents the element in the i th row and the j th column in matrix \mathbf{K} , and F_i is the i th simulated measurement and x_j is the j th element in the state vector \mathbf{x}). Jacobians identify the sensitivity of observation to the retrieved parameters. According to the optimal estimation theory (Rodgers, 2000), the errors of the retrieved state vector also follow a Gaussian distribution. The posterior error covariance matrix $\hat{\mathbf{S}}$ closely relates to errors of the measurements and the *a priori*:

$$\hat{\mathbf{S}}^{-1} = \mathbf{K}^T \mathbf{S}_\epsilon^{-1} \mathbf{K} + \mathbf{S}_a^{-1}. \quad (3)$$

The square roots of the diagonal elements of $\hat{\mathbf{S}}$ are the one sigma errors for the corresponding retrieved parameters.

The information content in the measurement for each retrieval parameter is often characterized in terms of averaging kernel (Frankenberg et al., 2012; Geddes and Bösch, 2015; Hasekamp and Landgraf, 2005; Holzer-Popp et al., 2008; Martynenko et al., 2010; Wang et al., 2014; Xu and Wang, 2015). By definition, the averaging kernel is the derivative of the posterior state vector with respect to the true state:

$$\mathbf{A} = \frac{\partial \hat{\mathbf{x}}}{\partial \mathbf{x}} = \left(\mathbf{K}^T \mathbf{S}_\epsilon^{-1} \mathbf{K} + \mathbf{S}_a^{-1} \right)^{-1} \mathbf{K}^T \mathbf{S}_\epsilon^{-1} \mathbf{K}. \quad (4)$$

The closer the averaging kernel matrix \mathbf{A} is to a unity matrix, the more perfect the retrieval. If \mathbf{A} is a null matrix, no information can be gained from the observation. The degree of freedom for signal (DFS), one scalar quantity that can quantify the information content in the

retrieval, is defined as the trace of averaging kernel matrix \mathbf{A} :

$$\text{DFS} = \text{trace}(\mathbf{A}). \quad (5)$$

Since the diagonal elements of matrix \mathbf{A} represent the sensitivity of each retrieved parameter to its corresponding truth, $A_{i,i} = 1$ ($A_{i,i}$ represents the i th row and the i th column element in matrix \mathbf{A} meaning DFS of the i th parameter in the state vector \mathbf{x}) indicates that x_i can be fully retrieved from the measurements, while $A_{i,i} = 0$ indicates that no information about x_i is given by measurements. As the result, DFS represents the number of independent pieces of information the measurements can provide. In this study, we focus on DFS and its components for aerosol information content analysis as well as retrieval error evaluated by $\hat{\mathbf{S}}$.

3. Satellite observation simulation

Applying the theory introduced in Section 2 to CAPI aerosol retrieval requires the knowledge of the measurement vector and the state vector, as well as their error covariance matrices. In this section we first briefly describe the CAPI observing characteristics and the forward model used to simulate CAPI observations. Then, we present the chosen parameters in the state vector and the assumptions of prior error and measurement error covariance matrices.

3.1. CAPI measurements and observation vector

CAPI collects observation in push broom mode with a spatial resolution 1.0 km and a wide FOV 16°. Table 1 shows some important characteristics about this satellite and two instruments on TanSat: CAPI and CDS. In the simulation, we assume Gaussian response function with full width at half maximum of 10 nm for all channels. Since the 1375-nm band of CAPI is mainly used for cirrus detection, it is not included in our measurement vector. DOLP is observed in 670-nm and 1640-nm channels with three polarizers placed 60° between each axial direction. To meet the mission requirements, TanSat will perform several observation tasks with different scanning configurations. Over land, the satellite mainly performs principal-plane nadir scans. Over ocean where surface reflectance is relatively lower, the sun-glint mode is generally used to observe sun-glint spot in orbit. In this study, we focus our investigation on principal-plane nadir viewing.

In order to investigate potential increase of the aerosol information content due to DOLP measured by CAPI, we compare our analysis for two scenarios: (1) retrieval from reflectance-only observation, and (2) retrieval with additional polarized measurements. Hence, the observation vector in the first scenario can be defined as:

$$\mathbf{y} = [I_{380}, I_{670}, I_{870}, I_{1640}]^T, \quad (6)$$

in which I_{380} represents the simulated reflectance at TOA in the 380-nm band and the similar definitions are applied to other elements. In contrast, the observation vector in the second scenario is:

$$\mathbf{y} = [I_{380}, I_{670}, I_{870}, I_{1640}, \text{DOLP}_{670}, \text{DOLP}_{1640}]^T. \quad (7)$$

We simulate these reflectances and DOLP for viewing zenith angles (VZA) from 0° to 75° and relative azimuth angles (RAA) ranging from 0° to 180° to analyze the angular dependence of information content. To simplify the presentation of the results, we first show the analysis of these simulations for SZA of 20°. Our subsequent analysis focus on CAPI principal-plane nadir observations at extended SZAs between 40° and 75°.

3.2. Forward model

We use UNL-VRM to simulate the CAPI's observations. UNL-VRM was developed as a numerical testbed that combines linearized single-

Table 1
Characteristics of TanSat.

Instruments	CDS			CAPI				
Band name or number	O ₂ –A	CO ₂ weak	CO ₂ strong	1	2	3	4	5
Spectral range (nm)	758–778	1594–1624	2041–2081	365–408	660–685	862–877	1360–1390	1628–1654
Spectral resolution (nm)	0.044	0.12	0.16	– ^a				
Polarization angle (°)	– ^a			– ^a	0/60/120	– ^a	– ^a	0/60/120
SNR ^b	360	250	180	260	160	400	180	110
Spatial resolution (km)	1 × 2			1 × 1				
Scan range (°)	–30–10			–16–16				
Swath (km)	20			400				
Orbit type	Sun-synchronous							
Altitude (km)	700							
Inclination (°)	98							
Local time	13:30							

^a The symbol represents that the characteristic does not exist for the instrument.

^b SNR: Signal to noise ratio.

scattering code for spherical particles with vector linearized radiative transfer model (Wang et al., 2014). As in Wang et al. (2014), this testbed has been used to conduct a feasibility study in which the retrieval of aerosol properties is improved through a synergic use of two geostationary satellites. The testbed has also been used for evaluating aerosol information content contained in the ground-based remote sensing system (AERONET) (Wang et al., 2014; Xu and Wang, 2015). Its forward modeling part consists of a linearized Mie code, a vector linearized discrete ordinate radiative transfer model (VLIDORT) that can compute analytical weighting functions (Spurr, 2008), and a surface model calculating bidirectional reflectance or polarization distribution functions (BRDF/BPDF), as well as modules computing the molecular Rayleigh scattering and trace gas absorption. After inputting atmospheric profiles of pressure, temperature and trace gas mixing ratio, aerosol microphysical parameters and profile parameters, as well as surface model parameters, we can gain the Stokes vector:

$$\mathbf{I} = [I, Q, U, V]^T, \quad (8)$$

as well as Jacobians with respect to each aerosol parameter (x_i):

$$\frac{\partial \mathbf{I}}{\partial x_i} = \left[\frac{\partial I}{\partial x_i}, \frac{\partial Q}{\partial x_i}, \frac{\partial U}{\partial x_i}, \frac{\partial V}{\partial x_i} \right]^T. \quad (9)$$

Since DOLP is defined as

$$DOLP = -\frac{Q}{I}. \quad (10)$$

The corresponding Jacobians of DOLP can be calculated by:

$$\frac{\partial DOLP}{\partial x_i} = \frac{Q}{I^2} \frac{\partial I}{\partial x_i} - \frac{1}{I} \frac{\partial Q}{\partial x_i}. \quad (11)$$

These Jacobians are then used in the optimal estimation framework as presented in Section 2.

In all forward calculations, aerosol particles are assumed to be spherical with a bimodal lognormal particle size distribution function characterized by effective radius r_{eff} and effective variance v_{eff} for both fine mode and coarse modes (Hasekamp and Landgraf, 2005; Mishchenko et al., 2007; Waquet et al., 2009). The aerosol microphysical parameters, as part of the input for our forward model, also include complex refractive index for both modes. The shape of the aerosol extinction profile follows a quasi-Gaussian function that peaks at 2 km and has a 2-km width at the half maxima of aerosol extinction (Ding et al., 2016; Wang et al., 2014).

To characterize the surface reflectance, we use the BRDF products of MODIS (Lucht et al., 2000; Schaaf et al., 2002). The Ross-Li kernels in the

BRDF describe the isotropic, volumetric and geometric-optical surface scattering, respectively (Wanner et al., 1995; Wanner et al., 1997):

$$R_I(\lambda, \vartheta_v, \vartheta_0, \varphi) = f_{\text{iso}}(\lambda) + k_1(\lambda)f_{\text{geom}}(\vartheta_v, \vartheta_0, \varphi) + k_2(\lambda)f_{\text{vol}}(\vartheta_v, \vartheta_0, \varphi), \quad (12)$$

where λ is wavelength, ϑ_v , ϑ_0 , and φ represent viewing zenith angle, solar illumination zenith angle, and relative azimuth angle, respectively. For this study, the radiative transfer calculation is conducted for two types of surfaces representing soil and vegetation. The coefficients in Eq. (12), $f_{\text{iso}}(\lambda)$, $k_1(\lambda)$, and $k_2(\lambda)$ are derived from MODIS BRDF products for typical soil and vegetated surfaces interpolated to CAPI bands (as shown in Table 2). In addition, since the land surface BPDF is shown to be rather small compared to BRDF (Litvinov et al., 2011; Litvinov et al., 2010; Maignan et al., 2009; Nadal and Breon, 1999; Waquet et al., 2009), the surface polarized reflectance is not treated in this study and the impact of this treatment will be evaluated in a future study.

3.3. The state vector

The state vector \mathbf{x} consists of 14 parameters characterizing the fine and coarse aerosol modes: the total aerosol columnar volume concentration V ($\mu\text{m}^3\mu\text{m}^{-2}$), four parameters describing the wavelength dependence of the complex refractive index ($m_r - m_i$) for each mode, the effective radius r_{eff} and variance v_{eff} for both modes, and the fine mode volume fraction (fmf_v). Instead of explicitly retrieving refractive index at all wavelengths, we assume the real and imaginary parts of refractive index (m_r , m_i) on are functions of wavelength following Dubovik and King (Dubovik and King, 2000):

$$m_r(\lambda) = a_r^* \lambda^{b_r}, \quad (13)$$

$$m_i(\lambda) = a_i^* \lambda^{b_i}. \quad (14)$$

Table 2
BRDF parameters of each band defined for both soil and vegetation.

Band (nm)	$f_{\text{iso}}(\lambda)^a$	$k_1(\lambda)^b$	$k_2(\lambda)^c$
380	0.0256/0.0354 ^d	0.0148/0.0086	0.0039/0.0095
670	0.1981/0.0840	0.1110/0.0170	0.0303/0.0250
870	0.3154/0.2520	0.2251/0.2080	0.0144/0.0210
1640	0.4210/0.3070	0.1620/0.0890	0.0570/0.0690

^a $f_{\text{iso}}(\lambda)$ represent amplitude factors for Lambertian kernel, as expressed in Eq. (12) in the main text.

^b $k_1(\lambda)$ represent amplitude factors for Ross-thick kernel, as expressed in Eq. (12) in the main text.

^c $k_2(\lambda)$ represent amplitude factors for Li-sparse kernel, also as expressed in Eq. (12) in the main text.

^d The left value is for soil surface and the right value is for vegetation surface.

Table 3

Aerosol microphysical parameters of both the fine and coarse modes.

Mode	r_{eff} (μm) ^a	v_{eff}	m_r^b	m_i
Fine	0.13	0.92	1.444, 1.433, 1.428, 1.415	0.0041, 0.0057, 0.0066, 0.0095
Coarse	1.90	0.41	1.577, 1.559, 1.550, 1.530	0.0016, 0.0024, 0.0029, 0.0046

^a r_{eff} and v_{eff} denote the effective radius and effective variance, respectively.^b The refractive indices ($m_r - m_i$) are listed at 380 nm, 670 nm, 870 nm, and 1640 nm respectively.

The a_r, b_r, a_i , and b_i are the fitting coefficients and are included in the state vector. The derivations of their Jacobians are presented in our previous study (Hou et al., 2016).

The fine-mode aerosol is assumed to be water-soluble particles at relative humidity of 50% from the OPAC database (Hess et al., 1998), with which the refractive index of Eq. (14) is fitted. The size and refractive index parameters for coarse particles are the same as those used in Xu and Wang (2015). Table 3 summarizes the aerosol microphysical parameters at CAPI wavelengths. Similar to Xu and Wang (2015), we define three different scenarios of aerosol mixtures, namely fine-mode dominated, well-mixed, and coarse-mode dominated. The corresponding fractions of the fine-mode volume are defined as 0.8, 0.5, and 0.2, respectively. The aerosol loading in all scenarios are defined by a total AOD of 1.0 at 440 nm.

3.4. The *a priori* and measurement errors

According to optimal estimation theory, aerosol information content analysis requires a realistic characterization of the *a priori* error

covariance matrix \mathbf{S}_a and the measurement error covariance matrix \mathbf{S}_e . To define the uncertainty for the wavelength dependence of aerosol refractive index, we used the Aerosol Robotic Network (AERONET) daily averaged complex refractive index inversion product for Beijing_RADI site during 2013–2015 as the *a priori* uncertainty of refractive index coefficients: a_r, b_r, a_i and b_i . In total, 302 inversions with AOD at 440 nm larger than 0.4 are found, at which circumstance the inversion accuracy for refractive index can be guaranteed (Fig. 1a). After analyzing the distribution of refractive index data as a function of fmf_v , as shown in Fig. 1b–c, we group the AERONET data with $\text{fmf}_v < 0.2$ as the coarse mode and with $\text{fmf}_v > 0.7$ as the fine mode; some outlier data points (such as the m_i larger than 0.1 when fmf_v is from 0.3 to 0.4 in Fig. 1c) are excluded in the analysis. Applying Eqs. (13) and (14) in both data groups, we obtain the standard deviation for a_r, b_r, a_i and b_i as the *a priori* error for fine and coarse mode respectively. For other parameters, the *a priori* error are assumed as relative errors, which are 80% for r_{eff} and v_{eff} of both two modes and 100% for aerosol column volume concentration V and fmf_v (Xu and Wang, 2015). Table 4 shows the *a priori* errors for all retrieved aerosol parameters. Similar to the assumption in Dubovik

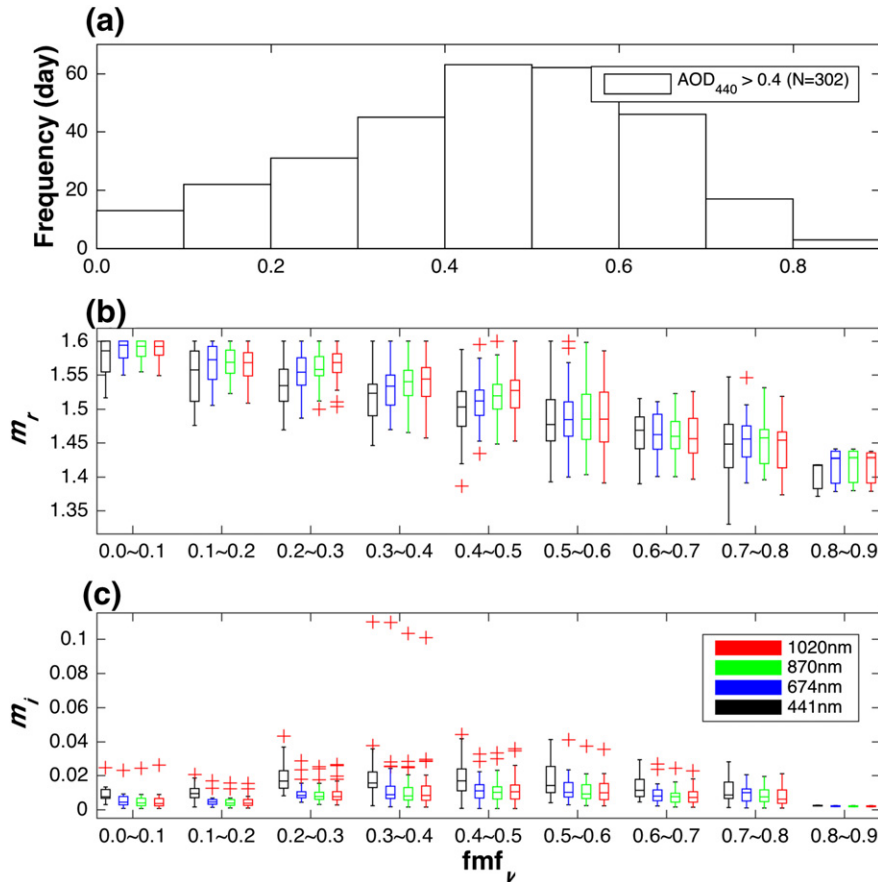


Fig. 1. (a) The histogram of fmf_v over Beijing_RADI site derived from AERONET daily inversion products during 2013–2015. (b) and (c) Climatology of aerosol complex refractive index ($m_r - m_i$) over Beijing_RADI site as the function of fmf_v . Four colorful boxes in each bin represent AERONET inversions in 4 bands, respectively. On each box, the central mark indicates the median, and the bottom and top edges of the box indicate the 25th (q1) and 75th (q3) percentiles, respectively. The whiskers extend from $q3 + 1.5 \times (q3 - q1)$ to $q1 - 1.5 \times (q3 - q1)$, and the rest data extending this range are plotted as outliers using the '+' symbol.

Table 4
The *a priori* error (%) of retrieved fine- and coarse-mode aerosol parameters.^a

Mode	V^b	fmf_v	r_{eff}	v_{eff}	a_r	b_r	a_i	b_i
Fine	100	100	80	80	19	574	195	46
Coarse	100	–	80	80	14	149	116	70

^a The errors are in terms of relative uncertainties and described by percentages.

^b The state vector is defined to include total aerosol volume and fmf_v instead of fine-mode volume and coarse-mode volume.

et al. (2000) and Xu and Wang (2015), we consider the *a priori* errors for retrieved parameters are independent between each other, so that S_a can be defined with zero off-diagonal elements.

We consider two components in the observation error: the uncertainties from both the measurement process and forward model parameters. Correspondingly, the measurement error covariance matrix used in the calculation of averaging kernel and posterior error is:

$$S_e = S_y + K_b S_b K_b^T, \quad (15)$$

in which S_y represents the uncertainty in measurement process, S_b is the error covariance matrix of surface model parameters in UNL-VRM, i.e. the spectral kernel factors for Ross-Li model, and K_b is the

weighting functions of measurement vector with respect to the model-input parameter vector \mathbf{b} that can be output from UNL-VRM directly. Based on the instrument characterization, the calibration accuracy is about 5% for CAPI reflectance detection. According to the research of Li et al. (2010) about some ground-based polarized radiometers (Li et al., 2010), the calibration uncertainty of DOLP is estimated about 0.005 to 0.01. We assume CAPI has the similar uncertainty of DOLP. Finally, in our study, we choose the relative error of 5% for reflectance I and absolute uncertainty of 0.01 for DOLP; this selection is also consistent with Xu and Wang (2015). Considering the limited knowledge of surface model and the accuracy of surface parameters, the relative uncertainties of BRDF kernel factors are assumed to 20%. Similarly, the errors for measurements and surface model parameters \mathbf{b} are also assumed to be non-correlated, so error covariance matrices S_y and S_b are diagonal matrix.

4. Results

Fig. 2a–f shows the simulated reflectance in four bands and DOLP in two bands at SZA of 20° over a vegetation surface for well-mixed aerosols. It is found that the TOA reflectance increases with wavelength due to larger surface reflectance at longer wavelength (Fig. 2g–i). The relatively large TOA reflectance at 380 nm results from strong Rayleigh

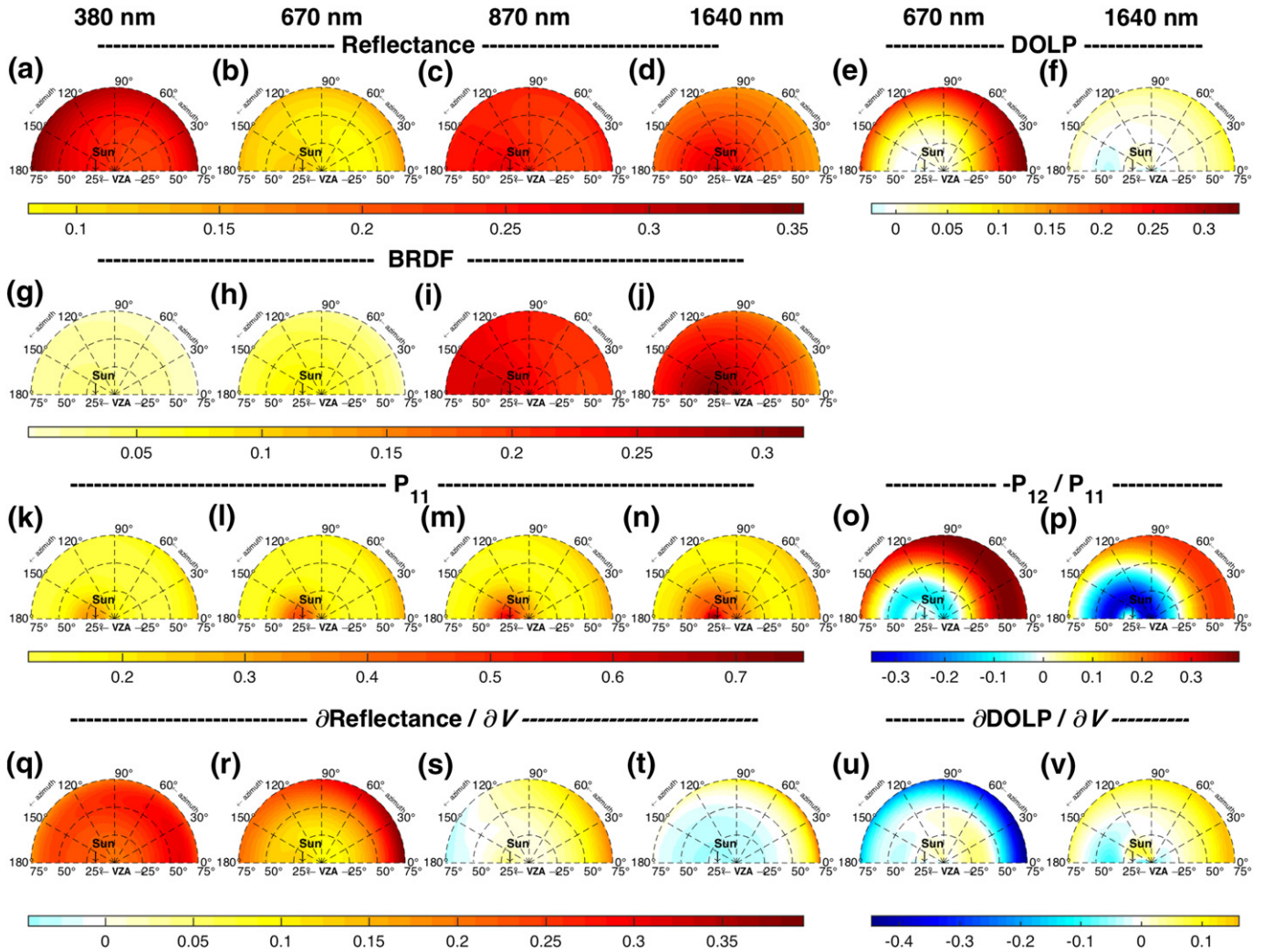


Fig. 2. Polar plots at 380 nm, 670 nm, 870 nm, 1640 nm (or 670 nm and 1640 nm for DOLP), respectively, of (a–d) simulated TOA reflectance, (e–f) DOLP at TOA, (g–j) surface BRDF, (k–n) aerosol scattering phase function P_{11} , (o–p) DOLP for light singly scattered by aerosols and calculated as $-P_{12}/P_{11}$ where P_{11} and P_{12} follow the traditional denotation of a 4×4 scattering phase matrix (Hansen and Travis, 1974), (q–t) Jacobians of TOA reflectance with respect to aerosol columnar volume V , and (u–v) Jacobians of DOLP at TOA with respect to V . All simulations are for a well-mixed aerosol model over a vegetation surface with SZA of 20°. The polar radius represents VZA from 0° to 75° and the polar angle is RAA from 0° to 180°.

scattering in UV band. Moreover, the reflectance around the backscattering direction is larger than other geometries due to enhanced surface reflectance and aerosol scattering at the backscattering region (Fig. 2g–i and k–n).

The geometric patterns of DOLP at TOA are determined by the DOLP of aerosol and Rayleigh scattering phase functions described as $-P_{12}/P_{11}$, where P_{11} and P_{12} follow the traditional denotation of the 4×4 scattering phase matrix (Hansen and Travis, 1974) shown in Fig. 2o–p. The decrease of DOLP in 670 nm with scattering angle results from a composite effect from both aerosol and Rayleigh scattering (Fig. 3e). DOLP is close to zero near 160° scattering angle where negative aerosol DOLP offsets the positive Rayleigh DOLP. When scattering angle continues increasing to 180° , DOLP from Rayleigh scattering is close to zero, and consequently, DOLP at TOA is mainly affected by DOLP from aerosol scattering, and thereby decreases (Fig. 2k–n). Smaller values of DOLP of aerosol scattering at 1640 nm result in smaller DOLP at TOA than that at 670 nm (Fig. 2o–p). Further analysis of Jacobians and information content for different aerosol parameters as a function of view geometries and aerosol scenarios are presented below.

4.1. Sensitivity of reflectance and DOLP to aerosol properties

The Jacobians of reflectance and DOLP at TOA with respect to total aerosol volume at different wavelengths are illustrated in Fig. 2q–v. The larger Jacobians are found at the viewing angles opposite to the sun (Fig. 2q–t), indicating that TOA reflectance is more sensitive to aerosol volume in these directions. This phenomenon is due to smaller surface reflectance at these geometries, which favors retrieval of aerosols (Fig. 2g–j). In contrast, at directions close to the incoming beam, large surface reflectance causes less sensitivity of TOA reflectance to aerosol properties. When VZA is large, away from SZA, Jacobians of reflectance become smaller with larger RAA. However, the sensitivity is larger at larger RAA when VZA is close to SZA.

In contrast, Jacobians of DOLP demonstrate distinct angular dependence from those of TOA reflectance. The magnitude of light DOLP at TOA is mainly affected by the scattering of aerosol and air molecules, and the depolarization effect of the underlying surface. Therefore, Jacobians of DOLP with respect to total aerosol volume manifest a complex interplay of aerosol scattering, Rayleigh scattering, and surface reflection. For example, DOLP in the 670-nm band is less affected by small surface reflectance (Fig. 3e). DOLP in this band decreases at most angles as aerosol volume increases (e.g. negative Jacobians in Fig. 2u). At 1640 nm, the depolarization of surface reflectance has larger impact on DOLP at TOA. Increase of aerosol tends to reduce such surface depolarization, leading to positive Jacobians at most angles in addition to the directions of back-scattering (Fig. 2v).

Moreover, Jacobians of reflectance and DOLP at TOA show distinct difference at different wavelengths. At longer wavelengths, larger surface reflectance and lower aerosol optical depth lead to smaller sensitivity of TOA reflectance to aerosol volume (compare Fig. 2q and r). This decrease of sensitivity is more obvious with larger fmf_v due to larger Angstrom exponent of fine aerosol. Similarly, DOLP at 1640 nm is smaller than 670 nm (Fig. 2e and f), due to both larger depolarization of surface reflectance (Fig. 2h and j) and smaller aerosol scattering DOLP (Fig. 3e) at 1640 nm. Therefore, Jacobians of DOLP at 670 nm and 1640 nm are distinguished by different effect of surface reflectance and aerosol scattering DOLP, as discussed in last paragraph.

In general, the magnitudes of DOLP Jacobians are similar or larger than that of reflectance Jacobians, indicating equal or more sensitivity of DOLP at TOA to aerosol properties. Therefore, it is expected to get more aerosol information and improve retrieval accuracy by adding these polarized measurements in the retrieval. In addition, the magnitudes of Jacobians differ among retrieved aerosol parameters, leading to different sensitivity and information content in the retrieval. We will compare the information content and retrieval accuracy of all retrieved parameters in the following section.

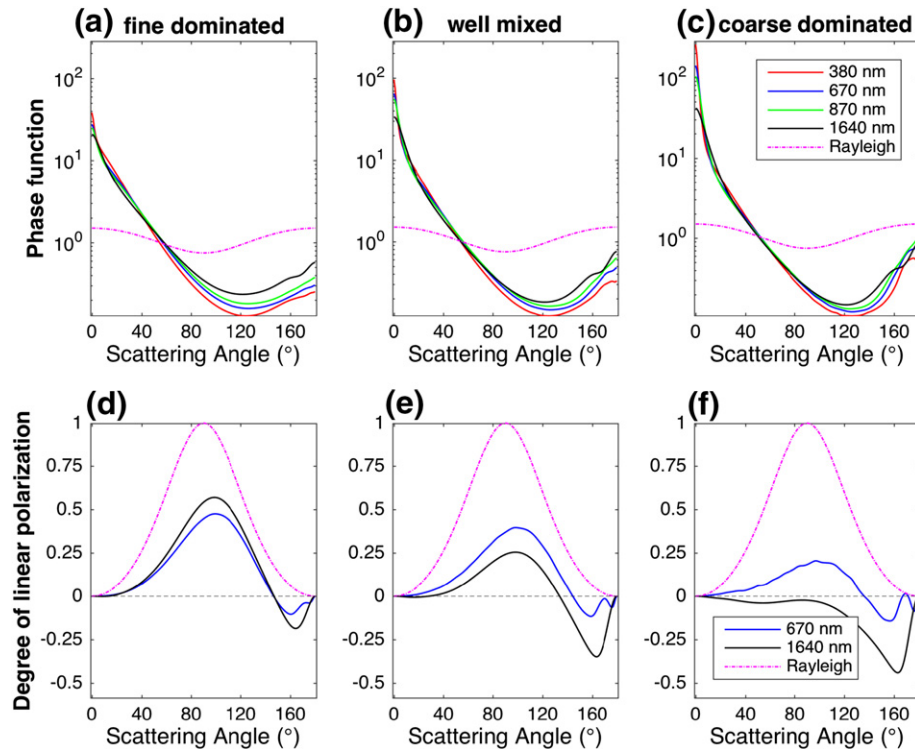


Fig. 3. Scattering phase function (P_{11}) and DOLP ($-P_{12}/P_{11}$) as a function of scattering angle for light singly scattered by molecular (Rayleigh scattering, magenta dash-dotted line) and aerosol at 380 nm (red line), 670 nm (blue line), 870 nm (green line), and 1640 nm (black line), respectively. Three columns (from left to right) represent three aerosol scenarios, respectively for fine dominated, well mixed and coarse dominated.

4.2. Aerosol information content analysis

Fig. 4a illustrates the angular distribution of aerosol information content in terms of total DFS for retrieving aerosol parameters from only CAPI reflectance measurements for well-mixed aerosol scenario. As the scattering angle increases, DFS values decrease at first and then increase slightly near backscattering. This variation is overall consistent with the change of total aerosol phase function (Fig. 2k–n) although large surface reflectance near backscattering (Fig. 2g–j) reduces aerosol information to some extent. The change of DFS with RAA is the same as Jacobians with respect to AOD shown in Section 4.1 (Fig. 2q–t); RAA could cause the difference of DFS as large as 0.5 when VZA is close to SZA. Moreover, in this scenario, DFS component is small at most angles for fine-mode b_i , coarse-mode a_i , fine-mode r_{eff} and v_{eff} , and coarse-mode v_{eff} . Therefore, CAPI measurements are not able to resolve these parameters, and we exclude these five parameters from the state vector in our following analysis. Fig. 5 shows the DFS of other nine parameters for well-mixed aerosol scenario. It is clear that b_i of coarse aerosol has the largest DFS of 0.7 (Fig. 5o) followed by a_i of fine aerosol with 0.4 DFS (Fig. 5i).

When DOLP is included in the retrieval, DFS reaches smallest near the direction of backscattering, due in part to the strong influence from large surface reflectance as well as small aerosol polarization at these angles (Fig. 2g–j and o–p). Consequently, DFS displays more complex variation with RAA at similar or smaller VZA than SZA. At these angles, especially for the wide FOV of CAPI (0° – 16°), different RAA could cause 1.6 or more DFS change. The information content for coarse-mode b_i is still largest with DFS values of 0.7 to 0.8 (Fig. 5p), followed

by the DFS values for fmf_v ranging from 0.5 to 0.65 (Fig. 5d). The DFS values for total aerosol volume (V), a_r , b_r and a_i for fine mode vary between 0.35 and 0.5 (Fig. 5b, f, h and j), and for the remaining parameters, a_r , b_r and r_{eff} for coarse mode, DFS values in the range from 0.2 to 0.35 DFS. It is concluded that the total aerosol information content mainly comes from parameters associated with fine-mode aerosols. Compared with 2 to 2.5 DFS in reflectance-only retrieval, combined reflectance and polarization observations can provide about 3 to 4.5 DFS at most viewing angles. Indeed, 6 (or 4) measurements can only provide <6 (or 4) pieces of information. Our analysis here is to identify the most informative parameters from 14 defined state parameters.

Overall, in average, DFS values are 0.75 and 0.6 respectively for b_i for coarse mode and fmf_v , when polarization data is used together with reflectance data to characterize well-mixed aerosol cases. The measurements also have some limited information about aerosol total volume and parameters of real part of refractive index of fine mode.

4.3. The improvement by adding polarization

For the purpose of analyzing the role of CAPI polarized measurements in aerosol retrieval, we also calculate the difference of total DFS after adding DOLP (right column of Fig. 4). Right column of Fig. 4 indicates that adding DOLP measurements can provide additional 1 to 1.8 independent pieces of information for aerosols at most angles regardless of aerosol types. Comparison among Fig. 4c, f and i reveals that the DFS improvement increases with decreasing fmf_v ; this is the result of large increment of DFS for coarse-mode aerosol while the

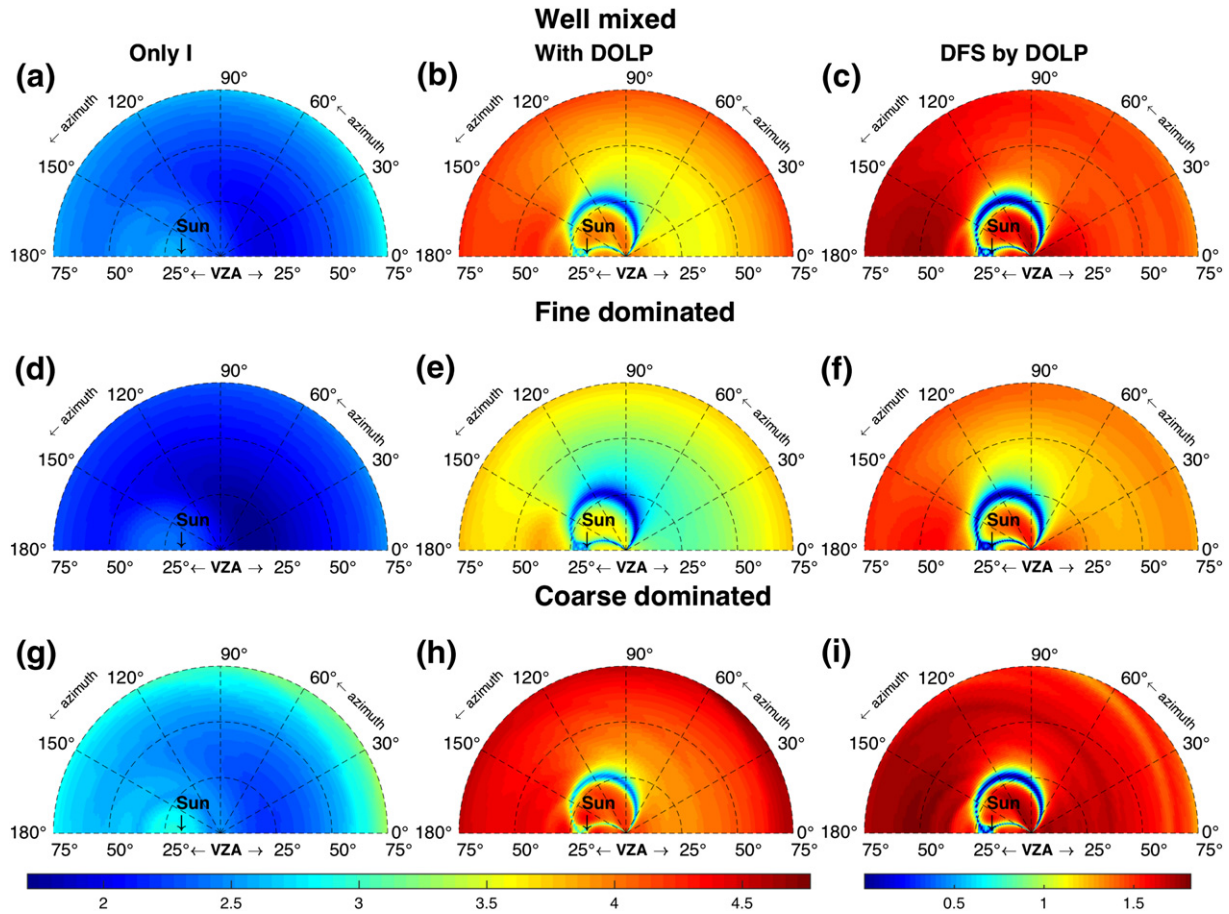


Fig. 4. Polar plots of DFS for retrieving 14 independent aerosol parameters under various aerosol conditions. Three rows correspond to the well-mixed aerosol scenario (a–c), fine-dominated scenario (d–f), and coarse-dominated scenario (g–i), respectively. Three columns (from left to right) represent aerosol DFS respectively from reflectance-only measurements, from both the reflectance and polarized measurements, and increased due to the addition of polarization. The solar zenith angle, polar radius, and polar angle are the same to those defined in Fig. 2.

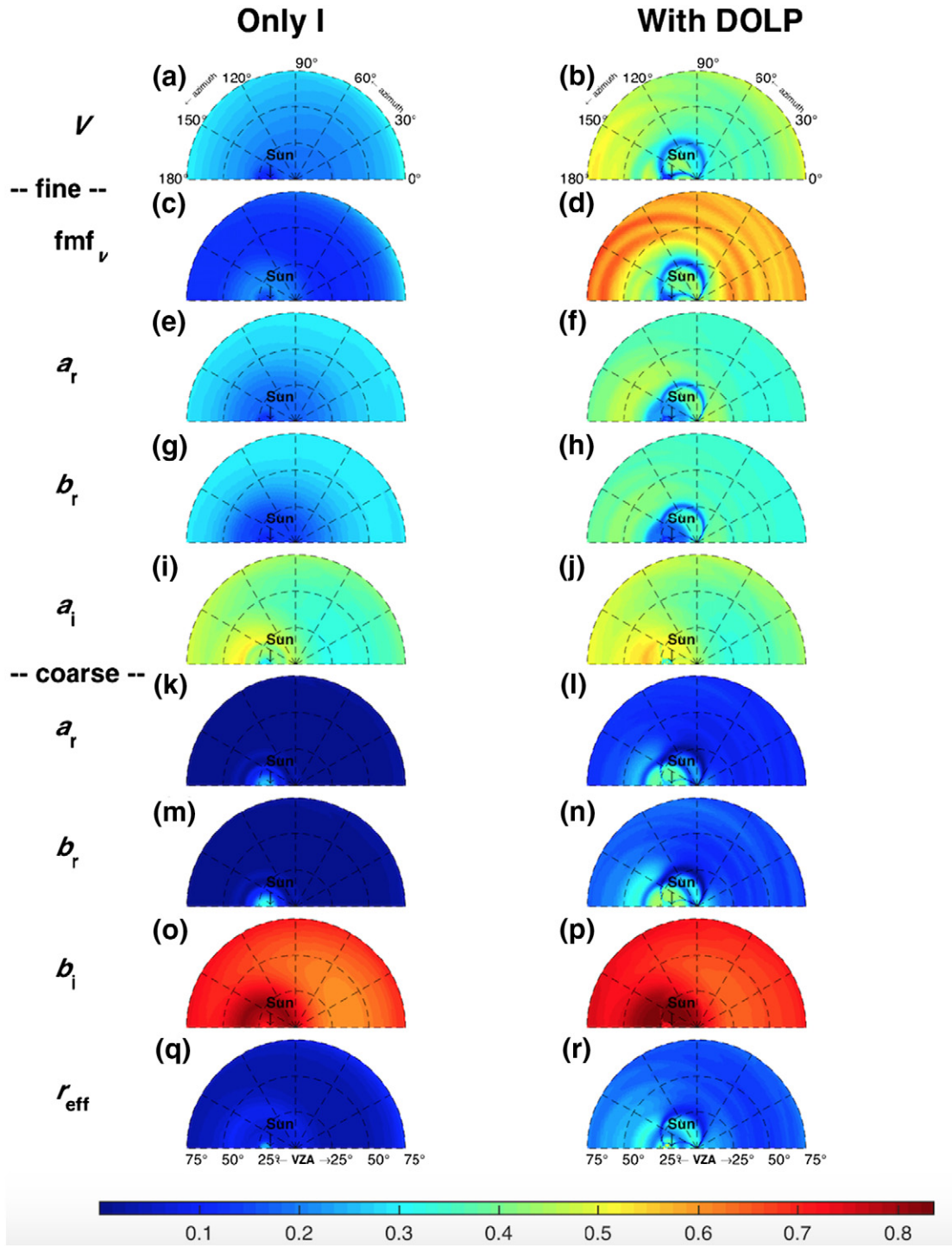


Fig. 5. Polar plots of individual DFS for each aerosol parameter defined in Table 3: V (panel a and b), fmf_v (c, d), fine-mode a_r (e, f), b_r (g, h), a_i (i, j), and coarse-mode a_r (k, l), b_r (m, n), b_i (o, p), and r_{eff} (q, r), respectively. The left column illustrates retrieval from reflectance-only measurements and the right column shows retrieval from both reflectance and polarized measurements. The solar zenith angle, the polar radius and polar angle are the same to those defined in Fig. 2.

information content for fine-mode parameters always retain large regardless of fmf_v .

Furthermore, in reflectance-only retrieval, total DFS values are larger at near-backscattering angles than other angles (Fig. 4a), whereas there is a ring with small DFS at these angles in the retrieval with polarization (Fig. 4b). This is the result of non-sensitivity of DOLP at TOA to aerosols (i.e. Jacobians of DOLP is zero, see Fig. 2u and v) in these directions. Hence, adding polarization cannot improve aerosol information content in these directions (i.e. almost zero value in Fig. 4c).

The improvement of DFS from DOLP for each retrieved parameter also can be found in Fig. 5. Total aerosol volume (V) and fmf_v best benefit from DOLP with additional 0.2 and 0.5 DFS, respectively. However, the information content of a_i of fine mode and b_i of coarse mode show little changes. One possible reason is the comparative sensitivity of TOA reflectance and DOLP with respect to imaginary part parameters, whereas there is large excess of DOLP Jacobians compared to reflectance Jacobians with respect to V and fmf_v (figures not shown).

5. Results for CAPI observation mode

TanSat carries out different tasks in different observation modes to meet the mission requirements. Over land, TanSat mainly scans near-nadir targets in the principal plane, which is called principal-plane nadir mode. In this mode, the VZAs are limited in its FOV of $\pm 16^\circ$ and SZA cannot be larger than 80° to achieve a sufficiently good SNR. Therefore, we analyze DFS from simulated CAPI measurements with VZAs from 0° to 16° and SZAs from 40° to 75° at two RAA (e.g., RAA = 0° and 180° in the principal plane) over both soil and vegetation for different aerosol scenarios. The results are shown in Fig. 6.

5.1. DFS analysis for principal-plane nadir mode

Fig. 6 manifests that DFS values for all aerosol parameters in CAPI reflectance-only retrieval over soil range from 1.5 to 2.0 for fine-dominated case, 1.7 to 2.2 for well-mixed case, and 1.8 to 2.4 for coarse-dominated case (whisker-box in blue color Fig. 6d–f). After accounting for DOLP into our retrieval, DFS values over soil can reach from 2.8 to 3.3 for fine-dominated case, 3.2 to 3.7 for well-mixed case, and 3.5 to 4.1 for coarse-dominated case, respectively (Fig. 6a–c). Therefore, CAPI DOLP measurements provide additional 1.3 to 1.7 pieces of aerosol information. In addition, it is found that the retrievals over vegetation (black whisker-box) have DFS about 0.5 larger than that over soil (blue whisker-box) due to low surface reflectance of vegetation.

Moreover, Fig. 6 also demonstrates that more aerosol information can be gained as SZA increases, which is the result of longer light path affected by aerosols for larger SZA. Furthermore, DFS for aerosol presents small variation with VZA within the FOV of CAPI, and this difference depends on the range of aerosol scattering phase function in the FOV. For example, as in Fig. 6a, the variability of DFS at SZA of 40° is larger than that at larger SZAs, which is the result of larger change of aerosol

scattering DOLP at the corresponding scattering angles (from 124° to 156°) (Fig. 3d–f). The largest change of DFS values with VZA can reach 0.3 for reflectance-only retrieval (Fig. 6d–f) and 0.4 retrieval with polarization (Fig. 6a–c), which are less than the variation of DFS caused by surface type and aerosol mixture.

5.2. DFS variation with solar zenith angle, AOD and fmf_v

According to the analysis above, aerosol information content of CAPI measurements varies with SZA and aerosol conditions. Thus, to investigate how aerosol type and SZA affect aerosol retrieval, we display the variation of aerosol information content from CAPI nadir observation (at 0° VZA) with fmf_v ranging from 0.02 to 0.98 at the same SZA with that used in Section 5.1 (from 40° to 75°) by keeping AOD 1.0 at 380 nm. Moreover, to describe the large variation of aerosol loading in real atmosphere, we also calculate the DFS and retrieval error when AOD ranges from 0.1 to 2.0 with the same set of fmf_v values.

Fig. 7a and b illustrate the contours of DFS values as a function of SZA and fmf_v with the same AOD (1.0 at 380 nm) in the retrieval with and without use of DOLP, respectively, and the difference between these two retrievals is shown in Fig. 7c. At the same SZA, when fmf_v increases, total aerosol DFS decreases in both retrievals. This is because coarse-mode aerosols are less optically significant than fine-mode aerosols. CAPI measurements contain less information about parameters of large particles (as shown in Fig. 5), and coarse-mode parameters are more difficult to retrieve than those for fine-mode aerosols. Thus, when fmf_v decreases, the information about coarse aerosol increases fast, while the information about fine aerosol remains high with little change, so the total information content increases. When SZA increases with the same fmf_v , aerosol information content increases slightly due to longer light path, as we discussed in Section 5.1. We note that for SZA smaller than 70° , DOLP provides the largest information content

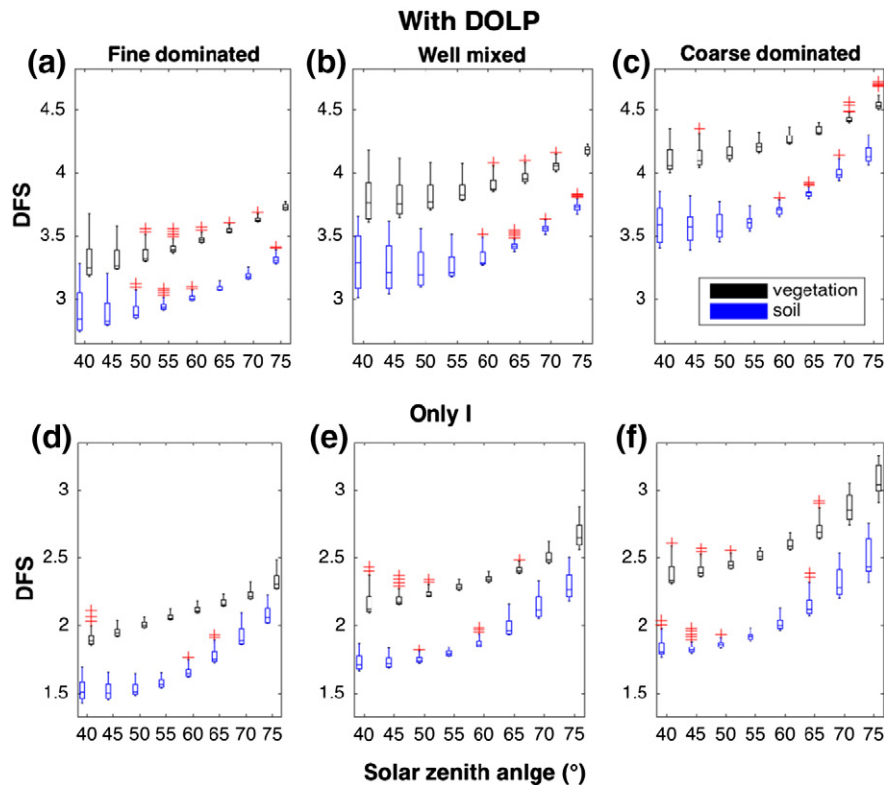


Fig. 6. The statistical DFS of CAPI observations as a function of SZA from 40° to 75° . Three columns correspond to three aerosol scenarios: fine-dominated, well-mixed, and coarse-dominated. The upper row demonstrates DFS of both reflectance and polarization measurements and the lower row for reflectance-only measurements. Also included in each panel are two surface types soil (black) and vegetation (blue). The symbol in each box-whisker is the same to that in Fig. 1.

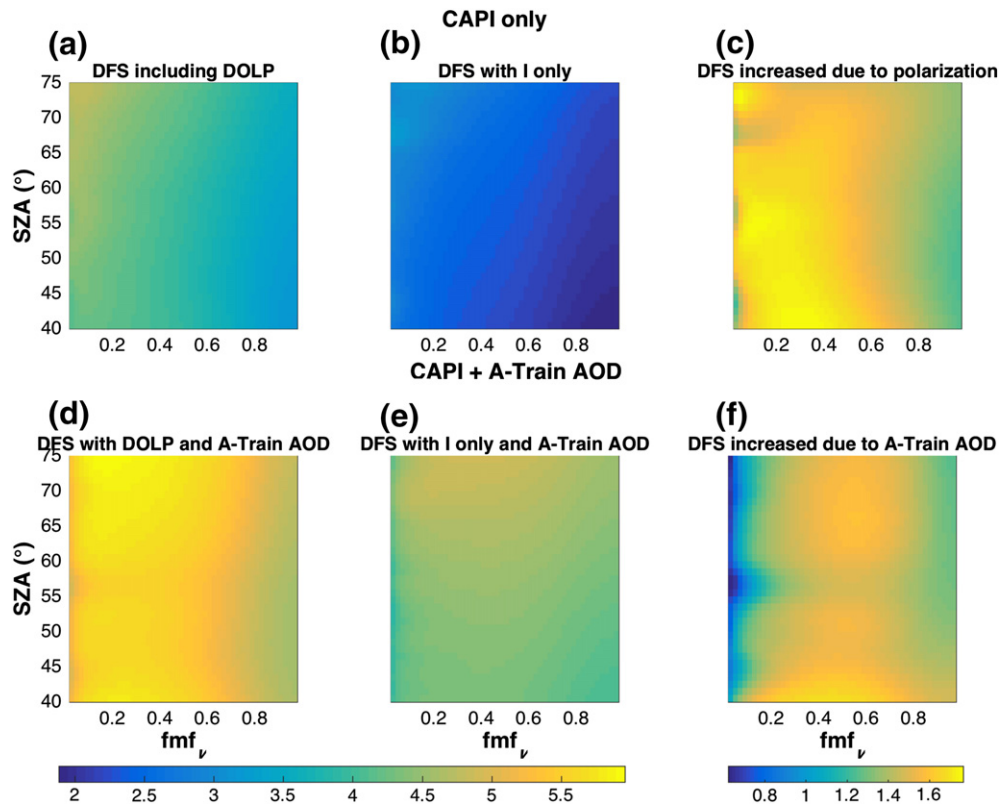


Fig. 7. Contours of DFS of various combinations of CAPI measurements as a function of SZA and fmf_v ; measurements of CAPI spectral reflectance at 380, 670, 870 and 1640 nm, and DOLP at 670 and 1640 nm (a), CAPI reflectance-only measurements (b), CAPI reflectance and DOLP plus A-Train AODs (d), and CAPI reflectance-only measurements plus A-Train AODs (e). Increases of DFS by adding DOLP or by adding A-Train AODs are shown in panels (c) and (f). All simulations are performed with 380-nm AOD of 1.0 and for a vegetation surface at nadir viewing.

(> 1.7 DFS, Fig. 7c) at fmf_v ranging from 0.2 to 0.4. For $fmf_v < 0.2$, the fine-mode AOD becomes so small that the decrease of fine aerosol information exceeds the increase of coarse aerosol information as fmf_v decreases. The change of additional DFS from DOLP with SZA depends more on aerosol scattering DOLP than the light path. When coarse aerosol dominates ($fmf_v < 0.4$), aerosol scattering DOLP decreases as SZA increases (scattering angle decreases, Fig. 3f), thus DFS decreases.

Similar patterns are also found in Fig. 9 (a–c). Regarding to the change of DFS with AOD, Fig. 9b show that DFS is < 1 for reflectance-only retrieval when AOD < 0.2. For a given fmf_v , total DFS increases with the increase of AOD due to more radiative impact from aerosol (Fig. 9a and b). However, this increase is larger for small fmf_v , than for large fmf_v , which is also attributed to less radiative effect of coarse-mode aerosol. We also notice that the improvement of DFS from DOLP reaches the largest (1.8 DFS) with $0.2 < fmf_v < 0.4$ and $1 < AOD < 2$ (Fig. 9c). If $fmf_v < 0.2$, DOLP provides the largest DFS for AOD from 1.2 to 1.6; after that, DOLP will not provide more information in spite of increasing AOD. This is because the information content about coarse mode from DOLP reaches a threshold and cannot be improved by increasing AOD.

The *a posteriori* error of each retrieved parameter as a function of fmf_v and SZA, or fmf_v and AOD in the retrieval with and without polarization is compared in Figs. 8 and 10, respectively. In our analysis, only those nine aerosol parameters with large information content in the retrieval is shown. As expected, posterior errors of fine-mode parameters decrease and errors of coarse aerosol parameters increase with increasing fmf_v , at given SZA and AOD except for low AOD conditions (central columns of Figs. 8 and 10). In reflectance-only retrieval, when SZA increases with a constant fmf_v , the errors of microphysical parameters for both modes remain nearly constant except for a_r and b_r of coarse mode, whose errors show slightly decrease at small fmf_v (left column of Fig. 8). In the retrieval with DOLP, the errors show more complex

change with SZA, especially for $0.2 < fmf_v < 0.4$, where coarse aerosol dominates and fine aerosol still contribute significant scattering (central column of Fig. 8). This fluctuation comes from aerosol polarization and related to the change of DOLP for coarse aerosol with the scattering angle. Nevertheless, DOLP has negligible effect on imaginary part of refractive index for both aerosol modes. When AOD increases, the error of each parameter decreases as a result of more aerosol information content from TOA reflectance and DOLP. However, this decreasing becomes less apparent as AOD increases to a fmf_v dependent threshold of 0.5 to 1.6, and then the *a posteriori* error will not be improved with increasing AOD (left and central columns of Fig. 10). The improvement for posterior errors by adding DOLP is the largest for total aerosol volume (20%) and fmf_v (40%) (Fig. 10a, b, d and e). The larger AOD and fmf_v , the more the improvement in fine-aerosol retrieval brought by polarization (or less fmf_v for coarse aerosol).

6. Synergy with A-train satellites

TanSat flies at a similar orbit of OCO-2 and has a possibility to join the A(fternoon)-Train satellite constellation. Question arises: can we combine aerosol products from other A-Train instruments (such as MODIS and CALIPSO) with TanSat observation to retrieve aerosol? For example, if AOD products of MODIS are used to constrain the CAPI's retrieval of aerosol properties, can the information content about aerosol from CAPI be improved? To address this question, we compare the DFS and the *a posteriori* error for retrievals before and after adding AOD at four CAPI bands in the observation vector. The observation error of AOD is assumed 15% at each wavelength to represent the uncertainty of MODIS AOD products (Levy et al., 2013). The uncertainties between different measurements are still assumed independent, and the *a priori* error covariance matrix is diagonal matrix.

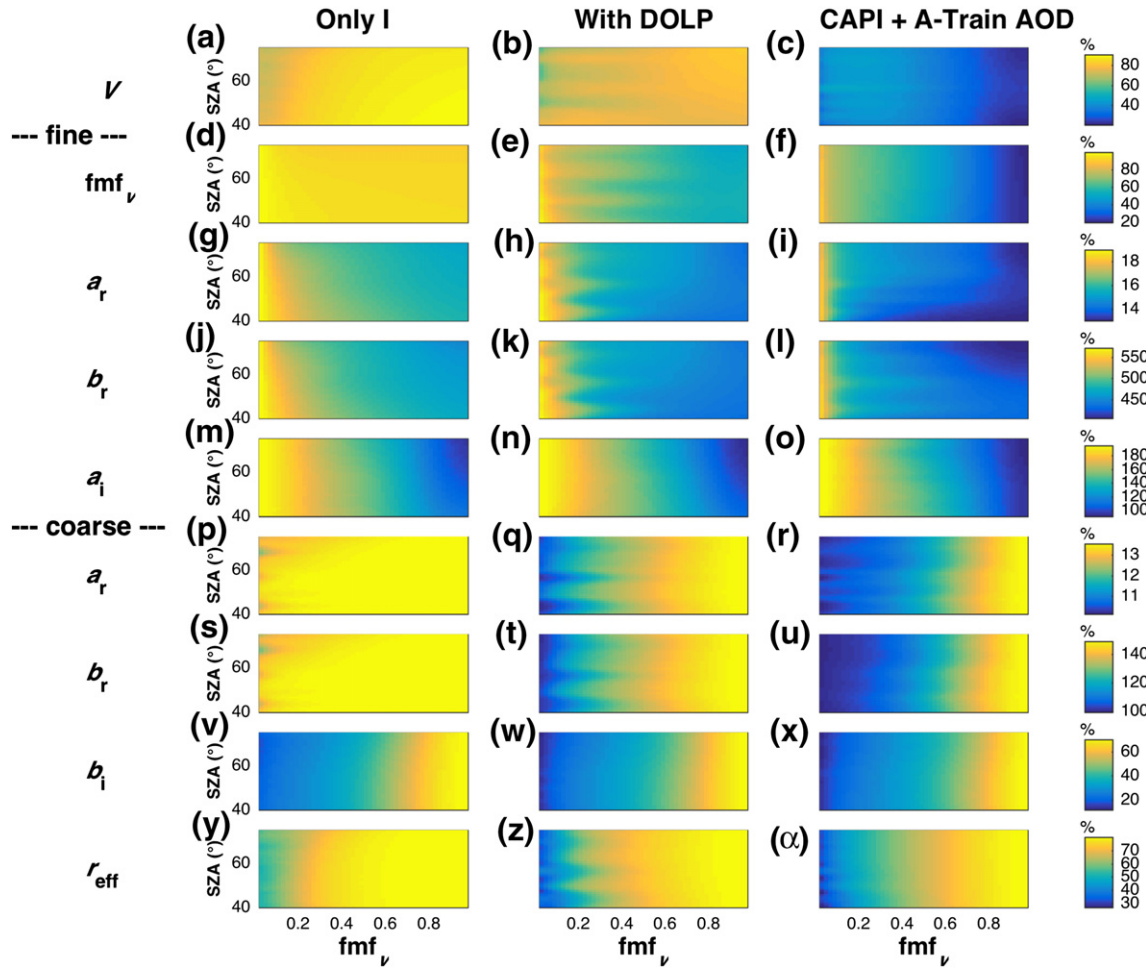


Fig. 8. Retrieval uncertainties for each retrieved aerosol parameter as a function of SZA and fmf_v , with the same AOD and surface reflectance of this figure: V (a–c), fmf_v (d–f), a_r (g–i), b_r (j–l) and a_i (m–o) for fine mode, a_r (p–r), b_r (s–u), b_i (v–x) and r_{eff} (y– α) for coarse mode, respectively. The three columns represent retrieval from only reflectance of CAPI observation, from both reflectance and polarization of CAPI observation, and from combined CAPI observation and A-Train AOD products. The errors are shown as the percentage ratio of *a posteriori* errors to *a priori* errors.

Fig. 7d and f shows that after adding AOD observation, aerosol DFS values can reach 4.5 to 5.9, an increase of 0.8 to 1.6 as compared to the retrieval from CAPI-only measurements including DOLP. When fmf_v increases, this increase of DFS becomes less, similar to the variation of DFS from CAPI-only measurements (Fig. 7f). If fmf_v is very low (<0.1), adding AOD observation makes little difference. In addition, adding AOD observation reduces the dependence of DFS on SZA. The increase of DFS from AOD observation shows negligible dependence on SZA especially for fmf_v from 0.2 to 0.8 (Fig. 7f). Similarly, this improvement as a function of fmf_v and AOD is displayed in Fig. 9d–f. The increased DFS reaches the largest with small AOD (<0.2) and demonstrates independence on fmf_v in addition to $fmf_v < 0.1$ or $fmf_v > 0.9$ (Fig. 9f). When AOD > 0.2 , the improvement from AOD observation is independent on AOD.

The right columns of Figs. 8 and 10 show *a posteriori* error for each retrieved aerosol parameter by including AOD in the observation vector. It is clear that the addition of AOD observations reduces the *a posteriori* error by 50% for total aerosol volume and 40% for fmf_v . For aerosol volume, the *a posteriori* error is reduced more for larger fmf_v , which is mainly caused by stronger sensitivity of AOD to fine-mode aerosols. Although the improvement of the *a posteriori* error for other parameters is less significant, the dependence of errors on SZA are reduced (Fig. 8i, l, o, r, u and x). According to Fig. 10f, i, l and o, the addition of AOD observations slightly reduces the dependence of the *a posteriori* error on AOD for fine-mode parameters. Oppositely, the errors reduction for coarse-mode a_r and b_r are more dependent on AOD.

Overall, if we use AOD observation at four wavelengths from other A-train satellites, we can gain more information about aerosol parameters, especially for total aerosol volume and fmf_v . The dependence of posterior error of each parameter on light path is also reduced so that retrieval is robust, regardless of the time and the season. In addition to small AOD with the largest additional DFS from AOD observation, the improvement of DFS keeps independent on AOD.

7. Summary and discussions

We estimate the aerosol microphysical property information content contained in the synthetic observations for CAPI. The top-of-the-atmosphere (TOA) reflectance and the degree of linear polarization (DOLP), as well as their weighting functions with respect to retrieved parameters, are simulated by the Unified Linearized Vector Radiative Transfer Model (UNL-VRM). Our simulation considers aerosols mixed by fine and coarse particles with various volume fractions over both vegetation and soil surfaces characterized by the Ross-Li Bidirectional Reflectance Distribution Function (BRDF). The information content of measurements can be interpreted by the degree of freedom for signal (DFS) and *a posteriori* error, which can be calculated from the *a priori* and measurement errors using the optimal estimation theory. To display the angular dependence of aerosol information content, observations at viewing zenith angle from 0° to 75° and relative azimuth angle from 0° to 180° , are simulated. Information content analysis is

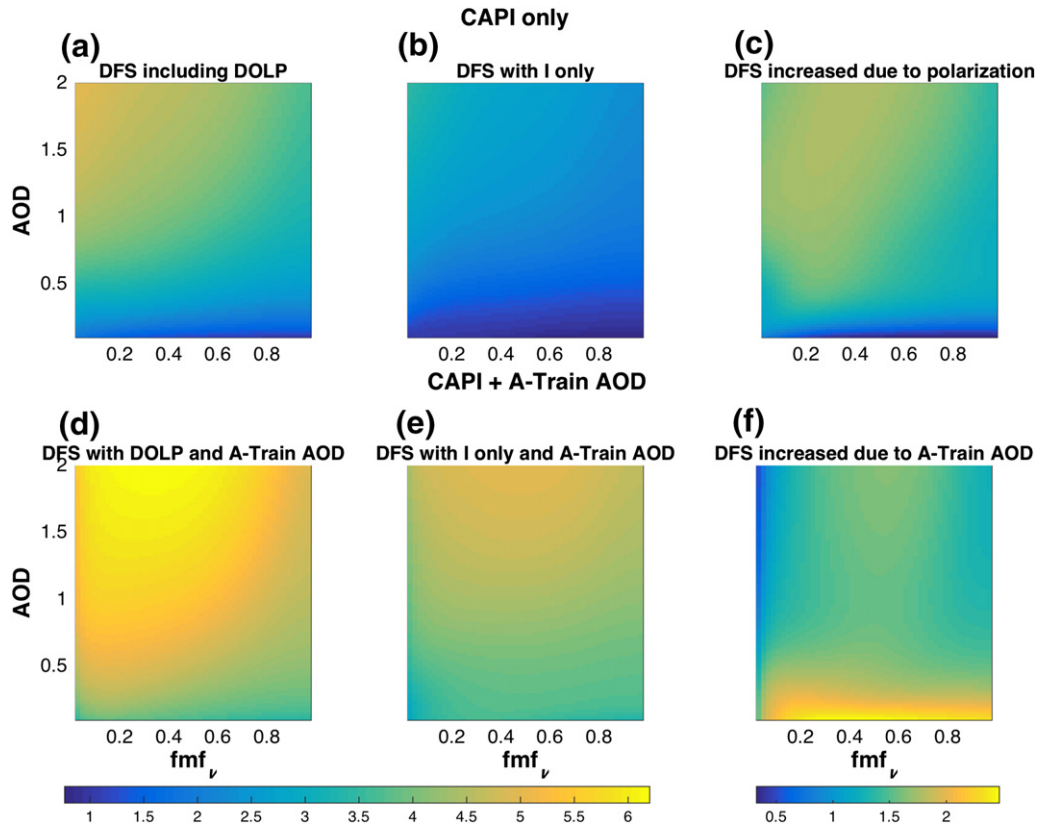


Fig. 9. Same as Fig. 7 but for DFS as a function of AOD and fmf_v . SZA and VZA are 50° and 0° , respectively.

conducted for various CAPI's observation modes (especially its main operational mode of principal-plane nadir observation) with the focus on the benefits of adding polarization measurements and the synergy of AOD from other A-train satellites.

Simulations show that both TOA reflectance and DOLP as well as their Jacobians change with the viewing geometry. At directions around backscattering, large surface reflectance leads to small DFS for retrieving aerosol information. Because of weak polarization of aerosol near backscattering angles, the sensitivity of TOA DOLP to aerosol volume is close to zero, leading to a ring of least DFS values at these directions even when DOLP measurements are added. Among those fourteen parameters defining bi-mode aerosol characteristics, large information content is found for aerosol total volume, imaginary part of refractive index of coarse mode (b_i) and fine mode volume fraction (fmf_v), with DFS larger than 0.4 at most angles. Adding DOLP measurements can provide additional 1 to 1.8 independent pieces of information at most angles, indicating that DOLP has the similar or more sensitivity than reflectance to aerosol properties; the increment arises mostly due to the high sensitivity of DOLP to aerosol volume, fmf_v , a_r and b_r of fine aerosol, whose DFS values all increase by 0.2 or more.

Detailed analysis is conducted for the most common observation mode of CAPI, the principal-plane nadir mode. In this mode, polarized measurements of CAPI can provide additional 1.3 to 1.7 independent pieces of information for aerosol, depending on the solar zenith angle, AOD, and fmf_v . In the range of SZA in our simulation (40° – 75°), the scattering phase function of coarse aerosols is always less than that of fine aerosols. Thus, large information content for fine aerosol parameters is always retained in the CAPI measurements. Consequently, when fmf_v decreases, aerosol DFS increases mainly for coarse-mode aerosol parameters. At larger solar zenith angle, the longer light path results in larger aerosol information content. When AOD is small (<0.2), aerosol DFS is relatively small regardless of the change of fmf_v . Although observation with larger AOD generally contains more aerosol information content, a threshold of AOD (0.5 to 1.6) exists, beyond which no more

aerosol information content can be obtained. The additional information content from polarization reaches the largest (1.7 DFS) when fmf_v ranges from 0.2 to 0.4. The larger fmf_v cause more information content and smaller posterior error for fine aerosol parameters but opposite patterns for coarse mode. In addition to a_r and b_r of coarse mode, posterior errors of other parameters are independent on solar zenith angle, albeit that DOLP can lead to some fluctuations.

Finally, we study the potential improvement for aerosol retrieval if AOD observations are available from other A-train satellites. AODs at four CAPI wavelengths are added into the CAPI measurement vector, which can result in the increase the DFS by 0.8 to 1.6. And the increased DFS shows smaller variation with SZA, indicating the dependence of aerosol retrieval accuracy on light path is reduced. The increase of DFS values due to the use of AOD data from other A-Train satellites are nearly constant regardless of AOD values except for small AOD conditions where the increase is the largest. The most significant reduction of *a posteriori* error by synergistic AOD observations is found for total aerosol volume and fmf_v , among all of the retrieval parameters. The analysis in this paper illustrates the high potential of CAPI on TanSat for characterizing aerosol properties, especially fine-mode aerosols, due to its inclusion of polarization measurements. Synergistic use of AOD products from other satellites can further improve CAPI's capability in the retrieval of aerosol microphysical properties. As a theoretical preparation for CAPI's algorithm for aerosol retrieval, this study only considered the most common land surface types, soil and vegetation, in the analysis. Deriving aerosol information over bright surface, such as desert and ice, is still important and difficult, and future analysis of CAPI's information content for aerosols over these bright surfaces will be conducted with real CAPI data. Realistic data from CAPI measurement can prove the conclusion of our manuscript. As of March 2017, CAPI is still subject to the orbiting test and onboard calibration (with solar and lunar sources). While CAPI has been collecting global data of all nine channels in normal condition, more calibration efforts are needed than expected. The TanSat research team plans to deliver L1B (radiance and

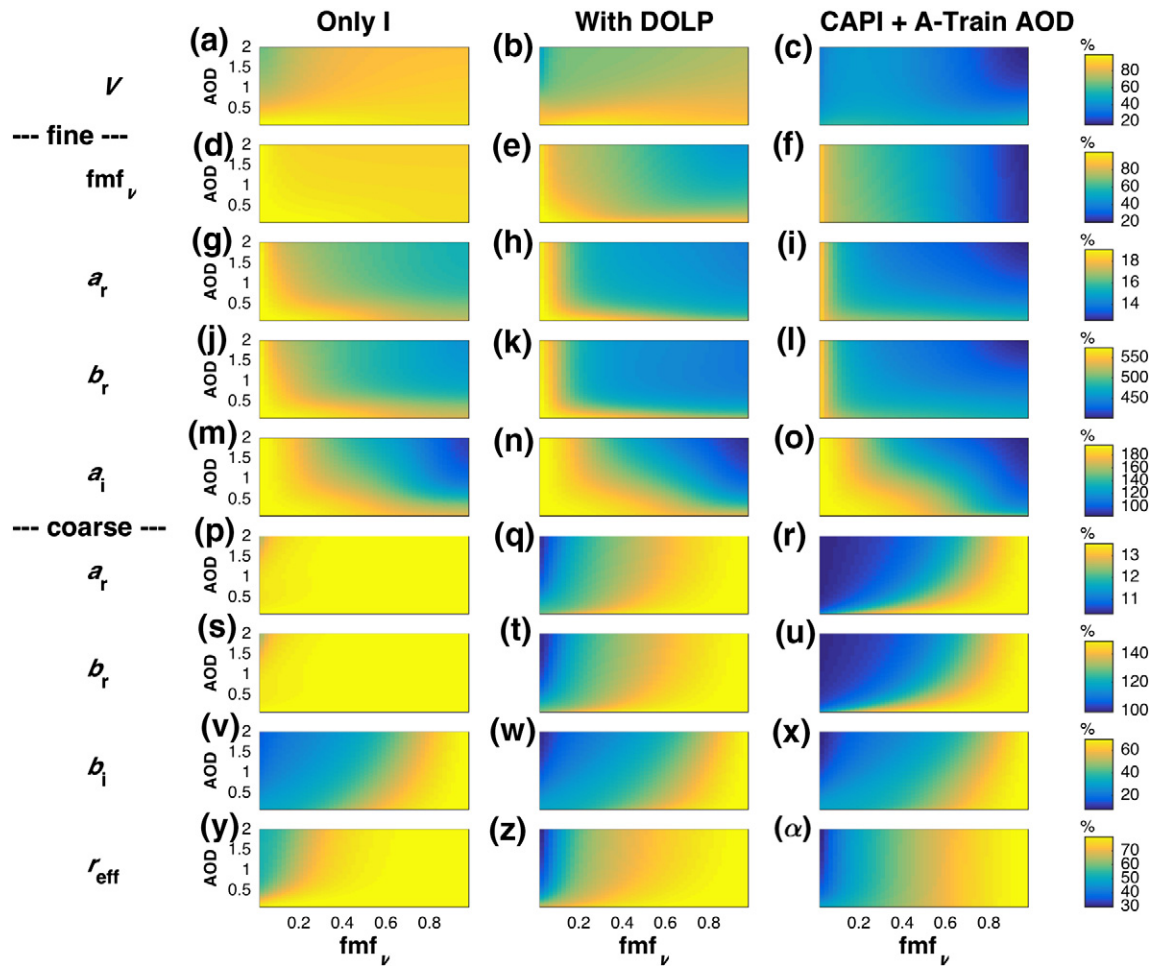


Fig. 10. Same as Fig. 9 but for a posteriori error as a function of AOD and fmf_v. SZA and VZA are 50° and 0°, respectively.

georeferenced) data of CAPI within six months after the calibration process is completed. The processes for conducting retrieval of aerosols will subsequently follow, and a combined use of radiance data from MODIS (as in (Tang et al., 2005)) and others sensors on A-Train with the CAPI's measurements to retrieve aerosols will also be further studied (as in Wang et al., 2014).

Acknowledgments

This study was supported by Chinese Academy of Sciences Strategic Priority program on space science (Grant No. XDA04077300) and National Natural Science Foundation of China (41375035). The University of Chinese Academy of Sciences (UCAS) also provides a scholarship for this study. We acknowledge Holland Computing Center and Office for Research and Economic Development in University of Nebraska-Lincoln for support of this research.

References

- Aben, I., Hasekamp, O., Hartmann, W., 2007. Uncertainties in the space-based measurements of CO₂ columns due to scattering in the Earth's atmosphere. *J. Quant. Spectrosc. Radiat. Transf.* 104, 450–459.
- Boesch, H., Baker, D., Connor, B., Crisp, D., Miller, C., 2011. Global characterization of CO₂ column retrievals from shortwave-infrared satellite observations of the orbiting carbon observatory-2 mission. *Remote Sens.* 3, 270–304.
- Butz, A., Hasekamp, O.P., Frankenberg, C., Aben, I., 2009. Retrievals of atmospheric CO₂ from simulated space-borne measurements of backscattered near-infrared sunlight: accounting for aerosol effects. *Appl. Opt.* 48, 3322–3336.
- Deuzé, J.L., et al., 2001. Remote sensing of aerosols over land surfaces from POLDER-ADEOS-1 polarized measurements. *J. Geophys. Res. Atmos.* 106, 4913–4926.

- Ding, S., Wang, J., Xu, X., 2016. Polarimetric remote sensing in oxygen A and B bands: sensitivity study and information content analysis for vertical profile of aerosols. *Atmos. Meas. Tech.* 9, 2077–2092.
- Dubovik, O., King, M.D., 2000. A flexible inversion algorithm for retrieval of aerosol optical properties from sun and sky radiance measurements. *J. Geophys. Res. Atmos.* 105, 20673–20696.
- Dubovik, O., Smirnov, A., Holben, B.N., King, M.D., Kaufman, Y.J., Eck, T.F., Slutsker, I., 2000. Accuracy assessments of aerosol optical properties retrieved from Aerosol Robotic Network (AERONET) sun and sky radiance measurements. *J. Geophys. Res. Atmos.* 105, 9791–9806.
- Dubovik, O., et al., 2011. Statistically optimized inversion algorithm for enhanced retrieval of aerosol properties from spectral multi-angle polarimetric satellite observations. *Atmos. Meas. Tech.* 4, 975–1018.
- Frankenberg, C., Hasekamp, O., O'Dell, C., Sanghavi, S., Butz, A., Worden, J., 2012. Aerosol information content analysis of multi-angle high spectral resolution measurements and its benefit for high accuracy greenhouse gas retrievals. *Atmos. Meas. Tech.* 5, 1809–1821.
- Geddes, A., Bösch, H., 2015. Tropospheric aerosol profile information from high-resolution oxygen A-band measurements from space. *Atmos. Meas. Tech.* 8, 859–874.
- Hansen, J.E., Travis, L.D., 1974. Light scattering in planetary atmospheres. *Space Sci. Rev.* 16, 527–610.
- Hasekamp, O.P., Landgraf, J., 2005. Retrieval of aerosol properties over the ocean from multi-spectral single-viewing-angle measurements of intensity and polarization: retrieval approach, information content, and sensitivity study. *J. Geophys. Res.* 110, 1–16.
- Herman, M., Deuzé, J.L., Devaux, C., Goloub, P., Bréon, F.M., Tanré, D., 1997. Remote sensing of aerosols over land surfaces including polarization measurements and application to POLDER measurements. *J. Geophys. Res. Atmos.* 102, 17039–17049.
- Hess, M., Koepke, P., Schult, I., 1998. Optical properties of aerosols and clouds: the software package OPAC. *Bull. Am. Meteorol. Soc.* 79, 831–844.
- Holzer-Popp, T., Schroeder-Homscheidt, M., Breitkreuz, H., Martynenko, D., Kluser, L., 2008. Improvements of Synergetic Aerosol Retrieval for ENVISAT. 8 pp. 7651–7672.
- Hou, W., Wang, J., Xu, X., Reid, J.S., Han, D., 2016. An algorithm for hyperspectral remote sensing of aerosols: 1. Development of theoretical framework. *J. Quant. Spectrosc. Radiat. Transf.* 178, 400–415.
- Houweling, S., Hartmann, W., Aben, I., Schrijver, H., Skidmore, J., Roelofs, G.-J., Breen, F.-M., 2005. Evidence of systematic errors in SCIAMACHY-observed CO₂ due to aerosols. *Atmos. Chem. Phys.* 5, 3003–3013.

- von Hoyningen-Huene, W., Freitag, M., Burrows, J.B., 2003. Retrieval of aerosol optical thickness over land surfaces from top-of-atmosphere radiance. *J. Geophys. Res. Atmos.* 108, 1–20.
- Hsu, N.C., Tsay, S.C., King, M.D., Herman, J.R., 2004. Aerosol properties over bright-reflecting source regions. *IEEE Trans. Geosci. Remote Sens.* 42, 557–569.
- Hsu, N.C., Tsay, S.C., King, M.D., Herman, J.R., 2006. Deep Blue retrievals of Asian aerosol properties during ACE-Asia. *IEEE Trans. Geosci. Remote Sens.* 44, 3180–3195.
- Hsu, N.C., et al., 2013. Enhanced Deep Blue aerosol retrieval algorithm: the second generation. *J. Geophys. Res. Atmos.* 118, 9296–9315.
- Kaufman, Y.J., Tanré, D., Remer, L.A., Vermote, E.F., Chu, A., Holben, B.N., 1997. Operational remote sensing of tropospheric aerosol over land from EOS moderate resolution imaging spectroradiometer. *J. Geophys. Res. Atmos.* 102, 17051–17067.
- Kokhanovsky, A.A., et al., 2010. The inter-comparison of major satellite aerosol retrieval algorithms using simulated intensity and polarization characteristics of reflected light. *Atmos. Meas. Tech.* 3, 909–932.
- Kokhanovsky, A.A., et al., 2007. Aerosol remote sensing over land: a comparison of satellite retrievals using different algorithms and instruments. *Atmos. Res.* 85, 372–394.
- Kuze, A., Suto, H., Nakajima, M., Hamazaki, T., 2009. Thermal and near infrared sensor for carbon observation Fourier-transform spectrometer on the Greenhouse Gases Observing Satellite for greenhouse gases monitoring. *Appl. Opt.* 48, 6716–6733.
- Levy, R.C., Remer, L.A., Mattoo, S., Vermote, E.F., Kaufman, Y.J., 2007. Second-generation operational algorithm: retrieval of aerosol properties over land from inversion of Moderate Resolution Imaging Spectroradiometer spectral reflectance. *J. Geophys. Res. Atmos.* 112, 1–21.
- Levy, R.C., Mattoo, S., Munchak, L.A., Remer, L.A., Sayer, A.M., Patadia, F., Hsu, N.C., 2013. The Collection 6 MODIS aerosol products over land and ocean. *Atmos. Meas. Tech.* 6, 2989–3034.
- Li, Z., Blarel, L., Podvin, T., Goloub, P., Chen, L., 2010. Calibration of the degree of linear polarization measurement of polarized radiometer using solar light. *Opt. Soc. Am.* 49, 1249–1256.
- Litvinov, P., Hasekamp, O., Cairns, B., Mishchenko, M., 2010. Reflection models for soil and vegetation surfaces from multiple-viewing angle photopolarimetric measurements. *J. Quant. Spectrosc. Radiat. Transf.* 111, 529–539.
- Litvinov, P., Hasekamp, O., Cairns, B., 2011. Models for surface reflection of radiance and polarized radiance: comparison with airborne multi-angle photopolarimetric measurements and implications for modeling top-of-atmosphere measurements. *Remote Sens. Environ.* 115, 781–792.
- Liu, Y., Yang, D., Cai, Z., 2013. A retrieval algorithm for TanSat XCO₂ observation: retrieval experiments using GOSAT data. *Chin. Sci. Bull.* 58, 1520–1523.
- Lucht, W., Schaaf, C.B., Strahler, A.H., 2000. An algorithm for the retrieval of albedo from space using semiempirical BRDF models. *Trans. Geosci. Remote Sens.* 38, 977–998.
- Maignan, F., Bréon, F.-M., Fédèle, E., Bouvier, M., 2009. Polarized reflectances of natural surfaces: spaceborne measurements and analytical modeling. *Remote Sens. Environ.* 113, 2642–2650.
- Martynenko, D., Holzer-Popp, T., Elbern, H., Schroedter-Homscheidt, M., 2010. Understanding the aerosol information content in multi-spectral reflectance measurements using a synergetic retrieval algorithm. *Atmos. Meas. Tech.* 3, 1589–1598.
- Mishchenko, M.I., et al., 2007. Accurate monitoring of terrestrial aerosols and total solar irradiance: introducing the glory mission. *Bull. Am. Meteorol. Soc.* 88, 677–691.
- Nadal, F., Breon, F.M., 1999. Parameterization of surface polarized reflectance derived from POLDER spaceborne measurements. *Trans. Geosci. Remote Sens.* 37, 1709–1718.
- Pachauri, R.K., M., L.A., C. W. Team (Eds.), 2014. IPCC, 2014: Climate Change 2014: Synthesis Report (151 pp).
- Rodgers, C.D., 2000. *Inverse Methods for Atmospheric Sounding: Theory and Practice*. World Scientific Publishing Co. Pte. Ltd.
- Schaaf, C.B., et al., 2002. First operational BRDF, albedo nadir reflectance products from MODIS. *Remote Sens. Environ.* 83, 135–148.
- Spurr, R., 2008. LIDORT and VLIDORT: linearized pseudo-spherical scalar and vector discrete ordinate radiative transfer models for use in remote sensing retrieval problems. In: Kokhanovsky, D.A.A. (Ed.), *Light Scattering Reviews*. 3. Springer, Berlin Heidelberg, pp. 229–275.
- Tang, J., Xue, Y., Yu, T., Guan, Y., 2005. Aerosol optical thickness determination by exploiting the synergy of TERRA and AQUA MODIS. *Remote Sens. Environ.* 94, 327–334.
- Torres, O., 2005. Total ozone mapping spectrometer measurements of aerosol absorption from space: comparison to SAFARI 2000 ground-based observations. *J. Geophys. Res.* 110, 1–12.
- Torres, O., Bhartia, P.K., Herman, J.R., Ahmad, Z., Gleason, J., 1998. Derivation of aerosol properties from satellite measurements of backscattered ultraviolet radiation: theoretical basis. *J. Geophys. Res. Atmos.* 103, 17099–17110.
- Torres, O., et al., 2007. Aerosols and surface UV products from ozone monitoring instrument observations: an overview. *J. Geophys. Res.* 112, 1–14.
- Wang, J., et al., 2014. A numerical testbed for remote sensing of aerosols, and its demonstration for evaluating retrieval synergy from a geostationary satellite constellation of GEO-CAPE and GOES-R. *J. Quant. Spectrosc. Radiat. Transf.* 146, 510–528.
- Wanner, W., Li, X., Strahler, A.H., 1995. On the derivation of kernels for kernel-driven models of bidirectional reflectance. *J. Geophys. Res.* 100, 21077–21089.
- Wanner, W., et al., 1997. Global retrieval of bidirectional reflectance and albedo over land from EOS MODIS and MISR data: theory and algorithm. *J. Geophys. Res. Atmos.* 102, 17143–17161.
- Waquet, F., Cairns, B., Knobelspiesse, K., Chowdhary, J., Travis, L.D., Schmid, B., Mishchenko, M.I., 2009. Polarimetric remote sensing of aerosols over land. *J. Geophys. Res.* 114, 1–23.
- Xu, X., Wang, J., 2015. Retrieval of aerosol microphysical properties from AERONET photopolarimetric measurements: 1. Information content analysis. *J. Geophys. Res. Atmos.* 120, 7059–7078.
- Xu, X., et al., 2015. Retrieval of aerosol microphysical properties from AERONET photopolarimetric measurements: 2. A new research algorithm and case demonstration. *J. Geophys. Res. Atmos.* 120, 7079–7098.
- Yokota, T., Yoshida, Y., Eguchi, N., Ota, Y., Tanaka, T., Watanabe, H., Maksyutov, S., 2009. Global concentrations of CO₂ and CH₄ retrieved from GOSAT: first preliminary results. *Scientific Online Letters on the Atmosphere*. 5, pp. 160–163.